



Improving Faraday rotation performance with block copolymer and FePt nanoparticle magneto-optical composite

ALEXANDER MILES,¹ YUE GAI,² PALASH GANGOPADHYAY,¹ XINYU WANG,² ROBERT A. NORWOOD,¹ AND JAMES J. WATKINS^{2,*}

¹College of Optical Science, University of Arizona, 1630 E. University Blvd., Tucson, AZ 85721, USA

²Department of Polymer Science and Engineering, University of Massachusetts, Amherst, 120 Governors Drive, Amherst, MA 01003, USA

* watkins@polysci.umass.edu

Abstract: Magneto-optical (MO) composites with excellent Faraday rotation (FR) response were fabricated using iron platinum (FePt) nanoparticles (NPs) and polystyrene-block-poly (2-vinyl pyridine) (PS-*b*-P2VP) block copolymers (BCPs). Gallic acid functionalized FePt NPs with average core diameters (d_{core}) of 1.9, 4.9, 5.7 and 9.3 nm have been selectively incorporated into a P2VP domain through hydrogen bonding interactions. The use of copolymer templates to selectively arrange the magnetic NPs guaranteed high MO performance with little trade-off in terms of scattering loss, providing a simple strategy to prepare functional materials for MO applications. As a result, Verdet constants of a 10 wt % loaded 4.9 nm FePt NP composite reached absolute magnitudes as high as $\sim 6 \times 10^4$ °/T-m at 845 nm, as determined by FR measurements at room temperature. At the same time, the MO figure-of-merit was as large as -25 °/T in these composites, indicating both excellent MO performance and transparency. The dependence of the nanocomposite FR properties on particle diameter, loading (from 0.1 wt % to 10 wt %) and composite nanostructure were systematically investigated at four infrared wavelengths (845, 980, 1310 and 1550 nm).

© 2017 Optical Society of America

OCIS codes: (230.2240) Faraday effect; (160.3820) Magneto-optical materials; (160.4890) Organic materials.

References and links

1. R. Bahuguna, M. Mina, J. W. Tioh, and R. J. Weber, "Magneto-Optic-based fiber switch for optical communications," *IEEE Trans. Magn.* **42**(10), 3099–3101 (2006).
2. L. D. Barron, *Molecular Light Scattering and Optical Activity*, 2nd ed. (Cambridge University Press, 2004), pp 264–272.
3. A. K. Zvezdin and V. A. Kotov, *Studies in Condensed Matter Physics. Modern Magneto-optics and Magneto-optical Materials*, (CRC Press, 1997), pp33–58.
4. P. Zu, C. C. Chan, G. W. Koh, W. S. Lew, Y. Jin, H. F. Liew, W. C. Wong, and X. Dong, "Enhancement of the sensitivity of magneto-optical fiber sensor by magnifying the birefringence of magnetic fluid film with loytsagnac interferometer," *Sens. Actuators B Chem.* **191**, 19–23 (2014).
5. M. Zayat, F. Del Monte, M. Del Puerto Morales, G. Rosa, H. Guerrero, C. J. Serna, and D. Levy, "Highly transparent γ -Fe₂O₃/Vycor-glass magnetic nanocomposites exhibiting Faraday rotation," *Adv. Mater.* **15**(21), 1809–1812 (2003).
6. S. Taccola, F. Greco, A. Zucca, C. Innocenti, C. de Julián Fernández, G. Campo, C. Sangregorio, B. Mazzolai, and V. Mattoli, "Characterization of free-standing PEDOT:PSS/iron oxide nanoparticle composite thin films and application as conformable humidity sensors," *ACS Appl. Mater. Interfaces* **5**(13), 6324–6332 (2013).
7. S. J. Chua and B. Li, *Optical Switches: Materials and Design* (Woodhead Publishing, 2010), pp 97–135.
8. B. J. H. Stadler and T. Mizumoto, "Integrated magneto-optical materials and isolators: a review," *IEEE Photonics J.* **6**, 0600215 (2015).
9. R. M. Silva, H. Martins, I. Nascimento, J. M. Baptista, A. L. Ribeiro, J. L. Santos, P. Jorge, and O. Frazão, "Optical current sensors for high power systems: a review," *Appl. Sci.* **2**(4), 602–628 (2012).
10. Z. Liu, H. Ukida, P. Ramuhalli, and K. Niel, *Integrated Imaging and Vision Techniques for Industrial Inspection* (Springer-Verlag London 2015), pp 483–536.
11. J. M. Caicedo, O. Pasqu, M. López-García, V. Canalejas, A. Blanco, C. López, J. Fontcuberta, A. Roig, and G. Herranz, "Magnetophotonic response of three-dimensional opals," *ACS Nano* **5**(4), 2957–2963 (2011).
12. J. C. Suits, "Faraday and Kerr effects in magnetic compounds," *IEEE Trans. Magn.* **8**(1), 95–105 (1972).

13. R. F. Ziolo, E. P. Giannelis, B. A. Weinstein, M. P. O'horo, B. N. Ganguly, V. Mehrotra, M. W. Russell, and D. R. Huffman, "Matrix-mediated synthesis of nanocrystalline $\text{ggr-Fe}_2\text{O}_3$: a new optically transparent magnetic material," *Science* **257**(5067), 219–223 (1992).
14. V. I. Belotelov, I. A. Akimov, M. Pohl, V. A. Kotov, S. Kasture, A. S. Vengurlekar, A. V. Gopal, D. R. Yakovlev, A. K. Zvezdin, and M. Bayer, "Enhanced magneto-optical effects in magnetoplasmonic crystals," *Nat. Nanotechnol.* **6**(6), 370–376 (2011).
15. V. I. Belotelov, L. E. Kreilkamp, I. A. Akimov, A. N. Kalish, D. A. Bykov, S. Kasture, V. J. Yallapragada, A. Venu Gopal, A. M. Grishin, S. I. Khartsev, M. Nur-E-Alam, M. Vasiliev, L. L. Doskolovich, D. R. Yakovlev, K. Alameh, A. K. Zvezdin, and M. Bayer, "Plasmon-mediated magneto-optical transparency," *Nat. Commun.* **4**, 1–7 (2013).
16. I. Crassee, J. Levallois, A. L. Walter, M. Ostler, A. Bostwick, E. Rotenberg, T. Seyller, D. van der Marel, and A. B. Kuzmenko, "Giant Faraday rotation in single- and multilayer graphene," *Nat. Phys.* **7**(1), 48–51 (2011).
17. R. Lewicki, J. H. Doty 3rd, R. F. Curl, F. K. Tittel, and G. Wysocki, "Ultrasensitive detection of nitric oxide at 5.33 microm by using external cavity quantum cascade laser-based Faraday rotation spectroscopy," *Proc. Natl. Acad. Sci. U.S.A.* **106**(31), 12587–12592 (2009).
18. M. A. Schmidt, L. Wondraczek, H. W. Lee, N. Granzow, N. Da, and P. St J Russell, "Complex Faraday rotation in microstructured magneto-optical fiber waveguides," *Adv. Mater.* **23**(22-23), 2681–2688 (2011).
19. R. Shimano, G. Yumoto, J. Y. Yoo, R. Matsunaga, S. Tanabe, H. Hibino, T. Morimoto, and H. Aoki, "Quantum Faraday and Kerr rotations in graphene," *Nat. Commun.* **4**, 1841 (2013).
20. P. Siddons, N. C. Bell, Y. Cai, C. S. Adams, and I. G. A. Hughes, "Gigahertz-bandwidth atomic probe based on the slow-light Faraday effect," *Nat. Photonics* **3**(4), 225–229 (2009).
21. P. Tartaj, T. González-Carreño, and C. J. Serna, "Single-step nanoengineering of silica coated maghemite hollow spheres with tunable magnetic properties," *Adv. Mater.* **13**(21), 1620–1624 (2001).
22. L. L. Beecroft and C. K. Ober, "Nanocomposite materials for optical applications," *Chem. Mater.* **9**(6), 1302–1317 (1997).
23. T. Yogo, T. Nakamura, W. Sakamoto, and S. Hirano, "Synthesis of transparent magnetic particle/organic hybrid film using iron-organics," *J. Mater. Res.* **15**(10), 2114–2120 (2000).
24. P. Hansen, C. Clausen, G. Much, M. Rosenkranz, and K. Witter, "Magnetic and Magneto-optical properties of rare-earth transition-metal alloys containing Gd, Tb, Fe, Co," *J. Appl. Phys.* **66**(2), 756–767 (1989).
25. A. B. Villaverde, D. A. Donatti, and D. G. Bozini, "Terbium gallium garnet Verdet constant measurements with pulsed magnetic field," *J. Phys. C Solid State Phys.* **11**(12), L495–L498 (2001).
26. S. Y. Sung, X. Qi, and B. J. H. Stadler, "Integrating yttrium iron garnet onto nongarnet substrates with faster deposition rates and high reliability," *Appl. Phys. Lett.* **87**(12), 1–3 (2005).
27. R. V. Mikhaylovskiy, E. Hendry, and V. V. Kruglyak, "Ultrafast Inverse Faraday Effect in a Paramagnetic Terbium Gallium Garnet Crystal," *Phys. Rev. B* **86**(10), 100405 (2012).
28. H. Majeed, A. Shaheen, and M. S. Anwar, "Complete stokes polarimetry of magneto-optical faraday effect in a terbium gallium garnet crystal at cryogenic temperatures," *Opt. Express* **21**(21), 25148–25158 (2013).
29. D. E. Lacklison, G. B. Scott, H. I. Ralph, and J. L. Page, "Garnets with high magneto-optic figures of merit in the visible region," *IEEE Trans. Magn.* **9**(3), 457–460 (1973).
30. G. Scott, D. Lacklison, H. Ralph, and J. Page, "Magnetic circular dichroism and Faraday rotation spectra of $\text{Y}_3\text{Fe}_5\text{O}_{12}$," *Phys. Rev. B* **12**(7), 2562–2571 (1975).
31. V. Doormann, J. P. Krumme, and H. Lenz, "Optical and magneto-optical tensor spectra of bismuth-substituted yttrium-iron-garnet films," *J. Appl. Phys.* **68**(7), 3544–3553 (1990).
32. M. Laulajainen, P. Paturi, J. Raittila, H. Huhtinen, A. B. Abrahamsen, N. H. Andersen, and R. Laiho, " $\text{Bi}_x\text{Y}_{3-x}\text{Fe}_5\text{O}_{12}$ Thin films prepared by laser ablation for magneto-optical imaging of superconducting thin films," *J. Magn. Magn. Mater.* **279**(2-3), 218–223 (2004).
33. M. Veis, E. Lišková, R. Antoš, Š. Višňovský, N. Kumar, D. S. Misra, N. Venkataramani, S. Prasad, and R. Krishnan, "Polar and longitudinal magneto-optical spectroscopy of bismuth substituted yttrium iron garnet films grown by pulsed laser deposition," *Thin Solid Films* **519**(22), 8041–8046 (2011).
34. A. Lopez-Santiago, H. R. Grant, P. Gangopadhyay, R. Voorakaranam, R. A. Norwood, and N. Peyghambarian, "Cobalt ferrite nanoparticles polymer composites based all-optical magnetometer," *Opt. Mater. Express* **2**(7), 978 (2012).
35. K. Hayashi, R. Fujikawa, W. Sakamoto, M. Inoue, and T. Yogo, "Synthesis of Highly Transparent Lithium Ferrite Nanoparticle/polymer Hybrid Self-Standing Films Exhibiting Faraday Rotation in the Visible Region," *J. Phys. Chem. C* **112**(37), 14255–14261 (2008).
36. E. M. Moreno, M. Zayat, M. P. Morales, C. J. Serna, A. Roig, and D. Levy, "Preparation of Narrow Size Distribution Superparamagnetic," *Langmuir* **18**(12), 4972–4978 (2002).
37. M. Domínguez, D. Ortega, J. S. Garitaonandia, R. Litrán, C. Barrera-Solano, E. Blanco, and M. Ramírez-del-Solar, "Magneto-optic Faraday effect in maghemite nanoparticles/silica matrix nanocomposites prepared by the sol-gel method," *J. Magn. Magn. Mater.* **320**(20), e725–e729 (2008).
38. V. Bonanni, S. Bonetti, T. Pakizeh, Z. Pirzadeh, J. Chen, J. Nogués, P. Vavassori, R. Hillenbrand, J. Åkerman, and A. Dmitriev, "Designer magnetoplasmonics with nickel nanoferrromagnets," *Nano Lett.* **11**(12), 5333–5338 (2011).
39. M. Moocarme, J. L. Domínguez-Juárez, and L. T. Vuong, "Ultralow-intensity magneto-optical and mechanical effects in metal nanocolloids," *Nano Lett.* **14**(3), 1178–1183 (2014).

40. P. Gangopadhyay, R. Voorakaranam, A. Lopez-Santiago, S. Foerier, J. Thomas, R. A. Norwood, A. Persoons, and N. Peyghambarian, "Faraday rotation measurements on thin films of regioregular alkyl-substituted polythiophene derivatives," *J. Phys. Chem. C* **112**(21), 8032–8037 (2008).
41. A. Lopez-Santiago, P. Gangopadhyay, J. Thomas, R. A. Norwood, A. Persoons, and N. Peyghambarian, "Faraday rotation in magnetite-polymethylmethacrylate core shell nanocomposites with high optical quality," *Appl. Phys. Lett.* **95**(14), 143302 (2009).
42. Z. H. Zhou, J. M. Xue, H. S. O. Chan, and J. Wang, "Transparent magnetic composites of ZnFe₂O₄ nanoparticles in silica," *J. Appl. Phys.* **90**(8), 4169–4174 (2001).
43. H. Cui, M. Wang, W. Ren, Y. Liu, and Y. Zhao, "Highly Transparent Silica Monoliths Embedded with High Concentration Oxide Nanoparticles," *J. Sol-Gel Sci. Technol.* **66**(3), 512–517 (2013).
44. R. García, M. Ramírez-Del-Solar, J. M. González-Leal, E. Blanco, and M. Domínguez, "Improving Magneto-optical Faraday Effect of Maghemite/silica Nanocomposites," *Mater. Chem. Phys.* **154**, 1–9 (2015).
45. P. K. Jain, Y. Xia, R. Walsworth, and A. E. Cohen, "Surface plasmon resonance enhanced rotation enhancement in gold-coated iron oxide nanocrystals," *Nano Lett.* **9**, 1644 (2009).
46. L. Wang, C. Clavero, Z. Huba, K. J. Carroll, E. E. Carpenter, D. Gu, and R. A. Lukaszew, "Plasmonics and enhanced magneto-optics in core-shell co-ag nanoparticles," *Nano Lett.* **11**(3), 1237–1240 (2011).
47. M. J. Fernée, C. Sinito, Y. Louyer, C. Potzner, T.-L. Nguyen, P. Mulvaney, P. Tamarat, and B. Lounis, "Magneto-optical properties of trions in non-blinking charged nanocrystals reveal an acoustic phonon bottleneck," *Nat. Commun.* **3**, 1287 (2012).
48. G. Armelles, A. Cebollada, A. Garcia-Martin, and M. U. Gonzalez, "Magnetoplasmonics: magnetoplasmonics: combining magnetic and plasmonic functionalities," *Adv. Opt. Mater.* **1**(1), 10–35 (2013).
49. T. Y. Kim, Y. Yamazaki, and T. Hirano, "Magneto-optical properties of Bi-YIG nanoparticle with polymethacrylate matrix materials," *Phys. Status Solidi Basic Res.* **241**(7), 1601–1604 (2004).
50. A. Lopez-Santiago, P. Gangopadhyay, J. Thomas, R. A. Norwood, A. Persoons, and N. Peyghambarian, "Faraday rotation in magnetite-polymethylmethacrylate core-shell nanocomposites with high optical quality," *Appl. Phys. Lett.* **95**(14), 143302 (2009).
51. A. I. Savchuk, I. D. Stolyarchuk, V. V. Makoviy, and O. A. Savchuk, "Magneto-optical Faraday rotation of semiconductor nanoparticles embedded in dielectric matrices," *Appl. Opt.* **53**(10), B22–B26 (2014).
52. J. Bang, U. Jeong, Y. Ryu, T. P. Russell, and C. J. Hawker, "Block copolymer nanolithography: translation of molecular level control to nanoscale patterns," *Adv. Mater.* **21**(47), 4769–4792 (2009).
53. J. Y. Cheng, C. A. Ross, H. I. Smith, and E. L. Thomas, "Templated self-assembly of block copolymers: top-down helps bottom-up," *Adv. Mater.* **18**(19), 2505–2521 (2006).
54. E. A. Jackson and M. A. Hillmyer, "Nanoporous membranes derived from block copolymers: from drug delivery to water filtration," *ACS Nano* **4**(7), 3548–3553 (2010).
55. H. A. Klok and S. Lecommandoux, "Supramolecular materials via block copolymer self-assembly," *Adv. Mater.* **13**(16), 1217–1229 (2001).
56. A. V. Ruzette and L. Leibler, "Block copolymers in tomorrow's plastics," *Nat. Mater.* **4**(1), 19–31 (2005).
57. C. Tang, E. M. Lennon, G. H. Fredrickson, E. J. Kramer, and C. J. Hawker, "Evolution of block copolymer lithography to highly ordered square arrays," *Science* **322**(5900), 429–432 (2008).
58. T. Thurn-Albrecht, J. Schotter, G. A. Kästle, N. Emley, T. Shibauchi, L. Krusin-Elbaum, K. Guarini, C. T. Black, M. T. Tuominen, and T. P. Russell, "Ultrahigh-density nanowire arrays grown in self-assembled diblock copolymer templates," *Science* **290**(5499), 2126–2129 (2000).
59. A. C. Balazs, T. Emrick, and T. P. Russell, "Nanoparticle polymer composites: where two small worlds meet," *Science* **314**(5802), 1107–1110 (2006).
60. M. R. Bockstaller, R. A. Mickiewicz, and E. L. Thomas, "Block copolymer nanocomposites: perspectives for tailored functional materials," *Adv. Mater.* **17**(11), 1331–1349 (2005).
61. J. Kao, K. Thorkelsson, P. Bai, B. J. Rancatore, and T. Xu, "Toward functional nanocomposites: taking the best of nanoparticles, polymers, and small molecules," *Chem. Soc. Rev.* **42**(7), 2654–2678 (2013).
62. J. Y. Lee, R. B. Thompson, D. Jasnow, and A. C. Balazs, "Entropically driven formation of hierarchically ordered nanocomposites," *Phys. Rev. Lett.* **89**(15), 155503 (2002).
63. W. A. Lopes and H. M. Jaeger, "Hierarchical self-assembly of metal nanostructures on diblock copolymer scaffolds," *Nature* **414**(6865), 735–738 (2001).
64. Y. Zhao, K. Thorkelsson, A. J. Mastroianni, T. Schilling, J. M. Luther, B. J. Rancatore, K. Matsunaga, H. Jinnai, Y. Wu, D. Poulsen, J. M. J. Fréchet, A. P. Alivisatos, and T. Xu, "Small-molecule-directed nanoparticle assembly towards stimuli-responsive nanocomposites," *Nat. Mater.* **8**(12), 979–985 (2009).
65. L. Yao, Y. Lin, and J. J. Watkins, "Ultrahigh loading of nanoparticles into ordered block copolymer composites," *Macromolecules* **47**(5), 1844–1849 (2014).
66. D. P. Song, Y. Lin, Y. Gai, N. S. Colella, C. Li, X. H. Liu, S. Gido, and J. J. Watkins, "Controlled supramolecular self-assembly of large nanoparticles in amphiphilic brush block Copolymers," *J. Am. Chem. Soc.* **137**(11), 3771–3774 (2015).
67. D. P. Song, C. Li, N. S. Colella, W. Xie, S. Li, X. Lu, S. Gido, J. H. Lee, and J. J. Watkins, "Large-volume self-organization of polymer/nanoparticle hybrids with millimeter-scale grain sizes using brush block copolymers," *J. Am. Chem. Soc.* **137**(39), 12510–12513 (2015).
68. Y. Lin, V. K. Daga, E. R. Anderson, S. P. Gido, and J. J. Watkins, "Nanoparticle-driven assembly of block copolymers: a simple route to ordered hybrid materials," *J. Am. Chem. Soc.* **133**(17), 6513–6516 (2011).

69. S. G. Jang, E. J. Kramer, and C. J. Hawker, "Controlled supramolecular assembly of micelle-like gold nanoparticles in PS-b-P2VP diblock copolymers via hydrogen bonding," *J. Am. Chem. Soc.* **133**(42), 16986–16996 (2011).
70. S. G. Jang, A. Khan, C. J. Hawker, and E. J. Kramer, "Morphology evolution of PS-B-P2VP diblock copolymers via supramolecular assembly of hydroxylated gold nanoparticles," *Macromolecules* **45**(3), 1553–1561 (2012).
71. Q. Wei, Y. Lin, E. R. Anderson, A. L. Briseno, S. P. Gido, and J. J. Watkins, "Additive-driven assembly of block copolymer-nanoparticle hybrid materials for solution processable floating gate memory," *ACS Nano* **6**(2), 1188–1194 (2012).
72. D. P. Song, C. Li, W. Li, and J. J. Watkins, "Block copolymer nanocomposites with high refractive index contrast for one-step photonics," *ACS Nano* **10**(1), 1216–1223 (2016).
73. D. P. Song, C. Li, C. S. Nicholas, X. Lu, J.-H. Lee, and J. J. Watkins, "Thermally tunable metallodielectric photonic crystals from the self-assembly of brush block copolymers and gold nanoparticles," *Adv. Opt. Mater.* **3**(9), 1169–1175 (2015).
74. Q. Guo, X. Teng, and H. Yang, "Fabrication of magnetic FePt patterns from langmuir-blodgett films of platinum-iron oxide core-shell nanoparticles," *Adv. Mater.* **16**(15), 1337–1341 (2004).
75. R. Gerritsma, S. Whitlock, T. Fernholz, H. Schlatter, J. Luigjes, J. U. Thiele, J. B. Goedkoop, and R. J. C. Spreeuw, "Lattice of microtraps for ultracold atoms based on patterned magnetic films," *Phys. Rev. A* **76**(3), 033408 (2007).
76. T. Bublat and D. Goll, "Large-area hard magnetic L10-FePt nanopatterns by nanoimprint lithography," *Nanotechnology* **22**(31), 315301 (2011).
77. Q. Dong, G. Li, C. L. Ho, M. Faisal, C. W. Leung, P. W. T. Pong, K. Liu, B. Z. Tang, I. Manners, and W. Y. Wong, "A polyferroplatinyne precursor for the rapid fabrication of L1(0) -FePt-type bit patterned media by nanoimprint lithography," *Adv. Mater.* **24**(8), 1034–1040 (2012).
78. S. Sun, C. B. Murray, D. Weller, L. Folks, and A. Moser, "Monodisperse FePt nanoparticles and ferromagnetic fept nanocrystal superlattices," *Science* **287**(5460), 1989–1992 (2000).
79. S. Sun, "Recent advances in chemical synthesis, self-assembly, and applications of FePt nanoparticles," *Adv. Mater.* **18**(4), 393–403 (2006).
80. V. Nandwana, K. E. Elkins, N. Poudyal, G. S. Chaubey, K. Yano, and J. P. Liu, "Size and shape control of monodisperse FePt nanoparticles," *J. Phys. Chem. C* **111**(11), 4185–4189 (2007).
81. X. Wang, R. D. Tilley, and J. J. Watkins, "Simple ligand exchange reactions enabling excellent dispersibility and stability of magnetic nanoparticles in polar organic, aromatic, and protic solvents," *Langmuir* **30**(6), 1514–1521 (2014).
82. N. Borrelli, "Faraday rotation in glasses," *J. Chem. Phys.* **41**(11), 3289–3293 (1964).

1. Introduction

Magneto-optical (MO) materials have numerous high-end photonic applications in optical isolators and circulators, optical switches, high performance magnetic field sensors and satellite navigation systems [1–11]. Faraday rotation (FR) is one of the most important MO phenomenon, in which the applied magnetic field changes the polarization plane of propagating linearly polarized light by inducing a circular birefringence [1–3,7,12]. For materials with negligible light absorption, the FR performance is determined by the Verdet constant (V) in units of $^{\circ}/\text{T}\cdot\text{m}$. The polarization rotation angle (θ) is proportional to V multiplied by the propagation length (L) under unit field (B) ($\theta = VBL$).

Verdet constant depends strongly on wavelength, temperature and intrinsic material properties. The macroscopic response is determined by the interaction of the magnetic field with the net volumetric magnetic moment within the optical path, whereas the magnetic moment itself is determined by the inherent electronic structure and composition of the material. The strength of allowed MO transitions and relative alignment of molecular orbitals among different elements within a composite determine whether the response is diamagnetic, paramagnetic or ferromagnetic responses, with the resulting V differing from the sum of the individual contributions [12].

Transparent materials with large FR response at room temperature have been of great interest over the last few decades [13–21]. Acceptable MO performance in a composite generally requires the dispersion of a large volume fraction of MO nanoparticles, which often leads to light losses through scattering, thereby decreasing transparency and useful FR response [22,23]. Today's benchmark MO materials include ferromagnetic terbium gallium garnet (TGG, $\text{Tb}_3\text{Ga}_5\text{O}_{12}$) [24–28] and bismuth (Bi) doped yttrium iron garnet (Bi:YIG, $\text{Y}_2\text{Fe}_5\text{O}_{12}$) [29–33], targeting visible and near infrared (NIR) regimes, respectively. However, this family of materials containing rare-earth elements is usually produced as single crystals

in order to achieve millimeter-scale path lengths for excellent MO performance [27,29,31]. The high processing costs associated with high-quality crystal growth and limited achievable film thickness have restricted their broader utilization [26,32,33].

Recently, composites using magnetic nanoparticles (MNPs) dispersed in organic matrices have offered an alternative low-cost method for generating MO materials [34–39]. Properly surface modified paramagnetic nanofillers, together with selected photomonomers, have resulting in thin film composites with good transparency [40,41]. To balance the trade-off between high NP loading and decreased transparency, the small particle scattering loss need be taken into consideration and alleviated. For small particles, much smaller than the wavelength of light, Rayleigh scattering predominates; large scattering can arise when there are substantial (> 0.1) differences between the refractive indices of the polymer matrix and inorganic NP. In this case, it is a necessary to use small NPs (< 20 nm) that are evenly distributed in a pore-free polymer matrix [22,23]. The transmittance of the film follows Beer's law, which is exponentially dependent on both NP concentration and propagation length. Taken together, fine control of the NP fill fraction and dispersion, as well as film thickness, are essential to guarantee adequate film transparency.

Various systems including MNPs and silica sol-gel porous matrix blends [36,37,42–44], plasmonic enhanced shell MNPs [38,39,45–48], and homopolymer stabilized core-shell MNP composites [34,35,49–51] have been studied to understand both their scattering mechanisms and MO performance. Despite the high Verdet constants achieved in some of these composites, the resulting scattering from porous matrices produced by sol-gel methods [36,37,42] or aggregation of large NPs at higher concentrations [34,50] still limit the FR application of these materials at realistic length scales. Thus, it is essential to find other strategies that give uniform MO composite materials with precise control over the particle distribution and balance light losses and concentration of MO species.

Block copolymer (BCP) directed self-assembly of NPs with attractive physical qualities offers a “bottom-up” and innovative avenue for producing MO composite materials [52–58]. BCPs can microphase segregate into versatile periodic structures at the nanoscale, with facile control over the volume fraction and chemical nature of the two blocks [59–63]. Strong NP/BCP interactions have been shown to selectively integrate functional NPs into specific domains with desired size, filling fractions, and building block directions [64–70]. Resulting hybrid materials, with improved electric and optical properties, have been utilized in organic field effect transistor [71] and polymeric Bragg mirrors [72,73].

As the critical MO component in hybrid materials, iron platinum (FePt) NPs are of great interest due to their excellent chemical stability and demonstrated applications in high-density magnetic storage, bio-sensing and therapeutics [74–77]. Simultaneous synthesis and surface modification of size controlled FePt particles with diameter less than 10 nm allowed the construction of paramagnetic materials displaying unique size dependent properties [78–81]. Copolymer templates can selectively arrange the NPs to reduce light scattering and improve FR response by permitting control of the NP filling fraction and distribution. To date few efforts have been directed toward MO material fabrication using selective arrangement of nanoparticles into a BCP template.

In this work, we demonstrated a solution processable method to prepare MO materials with high Verdet constants at room temperature by integrating FePt NPs into a polystyrene-*block*-poly (2-vinyl pyridine) (PS-*b*-P2VP) template, as shown in Fig. 1. NPs with core diameters (d_{core}) from 1.9 to 9.3 nm were synthesized and modified with gallic acid (GA) to enable hydrogen-bonding interactions with the P2VP domains. The selective distribution of particles in the P2VP domain at the nanoscale reduced scattering and achieved large Verdet constants in conjunction with improved transparency compared to conventional composites. We systematically investigated the role of particle size, loading, and optical wavelength in the FR response of BCP based polymeric composites, thus demonstrating a new platform for high performance MO hybrid materials.

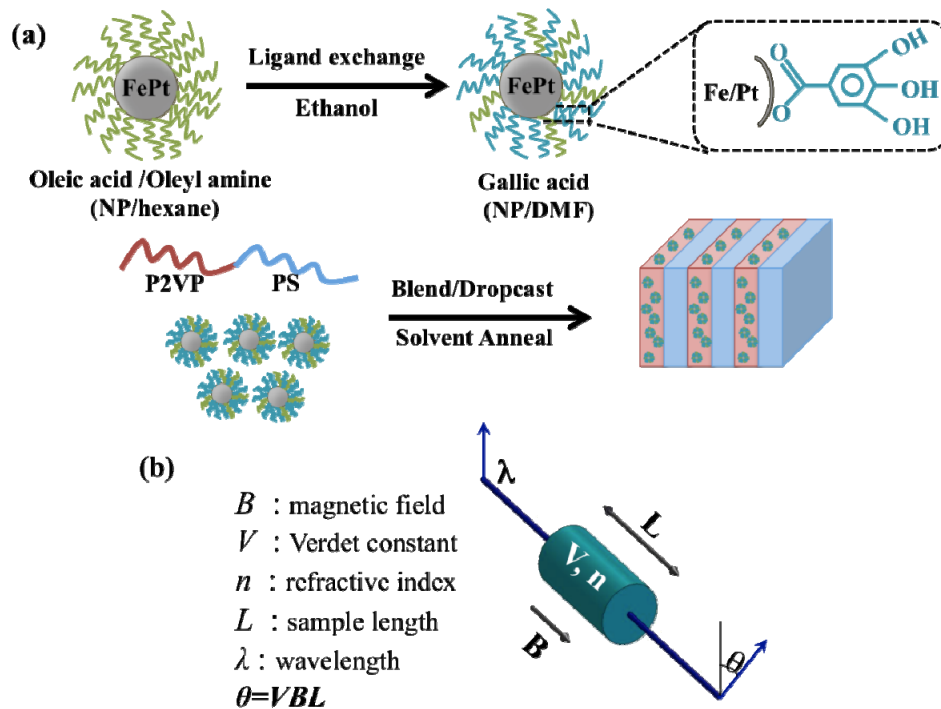


Fig. 1. (a) Surface modification of FePt NPs using gallic acid (GA) as a hydrogen bonding donor followed by selective NP dispersion in the P2VP domain within a symmetric PS-b-P2VP BCP template. (b) Illustration of Faraday rotation, the rotation of polarization angle depends on the Verdet constant (V) of medium, applied magnetic field (B) and path length of the light (L).

2. Experimental

2.1 FePt NP synthesis and surface modification

FePt NPs with core diameters from 1.9 to 9.3 nm were synthesized and surface modified following established procedures [80,81]. Typically hexane was removed from each 50 mg of as-prepared FePt NPs solution (10 mg/mL) under gentle nitrogen flow and 25 mg/mL GA (20 mL ethanol) solution was added immediately to the dried solids. The mixture was kept under sonication for two hours, and then left stirring overnight. The FePt-GA NPs were precipitated in a 200 mL 1:10 (v/v) ethanol/hexane mixture solvent with a neodymium magnet (2 inch \times 2 inch \times 1/2 inch, McMaster-Carr). Purified NPs were passed through a 0.2 μm PTFE filter and were stored in dimethylformamide (DMF).

2.2 Preparation of FePt NP/BCP blends

FePt NPs with different d_{core} with varied concentrations (from 0.1%, 0.5%, 1%, 2.5%, 5%, 7.5% to 10 wt %) were mixed with freshly prepared PS (102 kg/mol)-b-P2VP (97 kg/mol) (Polymer Source, Inc. (Montreal, Canada), $f_{\text{P2VP}} \sim 48.7\%$, PDI ~ 1.12) solution. The concentration of the blend solution was diluted to 2 wt % (10 mg solid content) with a mixture solvent of tetrahydrofuran (THF)/DMF ($v_{\text{T}}:v_{\text{D}} = 7:3$). The solution was then drop cast onto pre-cleaned glass slides (area $\sim 1'' \times 3''$ inch square) and dried at room temperature. The films were then annealed in saturated chloroform vapor at room temperature for at least 2 days, and then slowly dried in air for 1 day.

3. Measurements

Transmittance electron microscopy (TEM) was carried out with a JEOL 2000FX (accelerating voltage of 200kV) to investigate NP size and composite morphology. The samples were prepared by dropping dilute NP solution onto a thin carbon film supported by a copper grid. The size distribution of NPs was analyzed for a sample size of 300-400 particles with standard image analysis software (*Image J*). Electron diffraction images of NPs were calibrated with gold deposited carbon film. *Thermogravimetric analysis* (TGA) was performed on TA Instruments Q500, and the weight fraction of the FePt metal core was measured from 20 °C to 800 °C at 10 °C/min under an air purge flow. *X-ray diffraction* (XRD) was performed with a Panalytical X-pert X-ray powder diffractometer and X-ray reflectometer. The crystal structures of FePt NPs of various sizes were characterized with 5-10 mg FePt NPs powders with a 2θ scan from 30° to 110°. *Vibrating sample magnetometer* (VSM) measurements were performed on a Microsense EZ9 with FePt NPs copolymer composite films at room temperature. The obtained hysteresis loops from in-plane magnetization measurements are used to determine the particles' magnetization. *Ultraviolet-visible spectroscopy* (UV-vis) was performed on a Cary 5000 UV-Vis-NIR spectrometer to characterize the film absorption coefficient as a function of wavelength in the same regions of the thin films sampled in the thickness and Faraday rotation measurements. *Small angle X-ray scattering* (SAXS) was carried out on a Ganesha SAXS-LAB and performed with the Cu $K\alpha$ 0.154 nm line. Bulk film was carefully scraped and secured in the center of a washer with Kapton tape. *Microtoming* was performed on a Leica Ultracut UCT microtome at room temperature. Composite samples were prepared as 50 nm thin sections collected with carbon film on copper grids for microscopy, followed by subsequent iodine staining to increase P2VP domain contrast. *Profilometry* was performed on a Veeco Dektak 150 and the film thickness of dropcast film was determined by contact mode with a minimum of three scans per film.

Faraday rotation measurements. The Verdet constants were measured in a two-pass sinusoidal magnetic field driven homodyne apparatus using a NewFocus Nirvana 2017 auto-differential detector with efficient common-mode noise cancellation. This experiment is illustrated schematically in Fig. 2. This detector employed in conjunction with a lock-in amplifier, allowed for accurate measurement of small Faraday rotations. Due to the nonreciprocal nature of Faraday rotation, such a two-pass setup generates twice the rotation for a given magnetic field and cancels any rotation effect present that is reciprocal in nature. Inherent anisotropy in FePt NPs copolymer composites may generate such reciprocal rotations of the polarization as a result of circular birefringence and scattering. The sinusoidal output from the internal oscillator of the lock-in amplifier, a Stanford Research Systems SR830, is fed into a home-built low-noise amplifier/solenoid driver to create 20 to 400 gauss of sinusoidal magnetic flux density at the composite film. The magnetic fields are calibrated periodically using a Hall probe ac gauss meter. A polarization controller consisting of a half-wave plate and a high extinction-ratio linear polarizer prepared the light in a known polarization state. After a non-polarizing beam splitter (NPBS), the light is passed through the sample twice, yielding a rotation of the linear polarization state of 2θ , where θ is directly proportional to the sample thickness, applied magnetic field, and Verdet constant. The light is then spatially separated into vertically and horizontally polarized components (denoted s and p) by a Wollaston prism, focused by a singlet lens, and detected with an auto-differential detector. The detector used here is an InGaAs (1000-1600 nm) based Nirvana autobalanced front-end receiver, Model 2017 from New Focus. The wavelengths used in these experiments are 850 nm, 980 nm, 1310 nm, and 1550 nm (all distributed feedback semiconductor diode lasers). Auto-balanced phase-sensitive detection is used to reduce common-mode laser noise reference correction. The measured rotation is generally recovered as a phase change, a ratiometric quantity, unlike the more common traditional polarimetric method, i.e., through a polarizer/rotating analyzer.

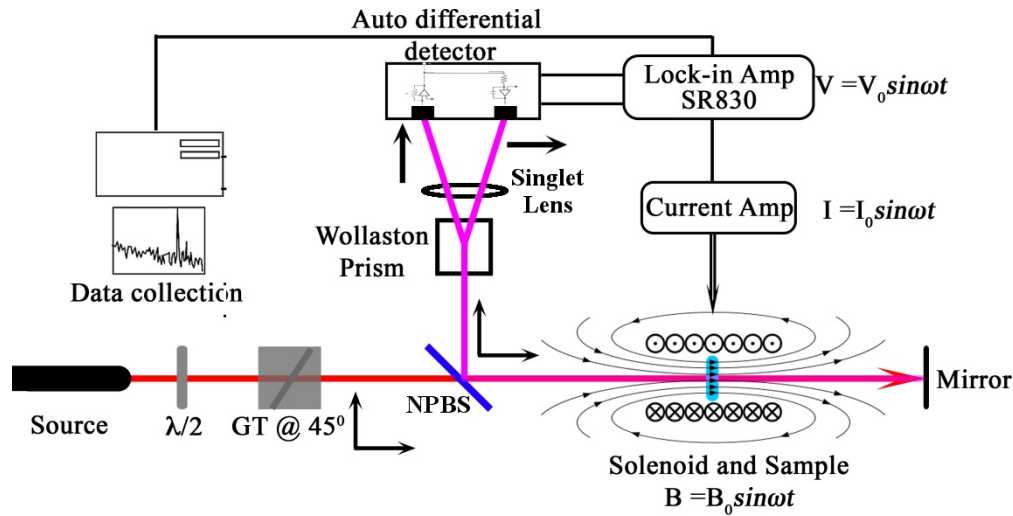


Fig. 2. Schematic drawing of the homodyne Faraday rotation measurement system with a sinusoidal magnetic field; the purple line represents the second pass through the sample; GT is a Glan Thomson polarizer and NPBS is a non-polarizing beam splitter. Black arrows along the optical path denote polarization states.

The Mueller matrix treatment applied to the measurement described in Fig. 2 yields the time-varying part of the signal on the Wollaston prism as $\theta_0 \sin \omega t$, with ω being the frequency of the magnetic field modulation. The Wollaston prism separates the two linearly polarized components, and the intensities falling on the two detectors can be described as:

$$I_t^h = kI_0 \sin(2n\theta_0 \sin(\omega t)), \quad I_t^v = kI_0 \sin\left(\frac{\pi}{2} - 2n\theta_0 \sin(\omega t)\right) \quad (1)$$

Here, n is the number of passes, and h and v denote horizontal and vertical states of polarization, respectively. Applying the Fourier-Bessel transform to the intensities falling on the differential detectors, leads to the following, in degrees:

$$\theta_0 = \frac{180}{\pi} \frac{|I_{ac}^h(\omega)_{rms} - I_{ac}^v(\omega)_{rms}|}{2ng_i(I_{dc}^h + I_{dc}^v)} \quad (2)$$

where θ_0 is the Faraday rotation and I is the measured intensity at the detector for the various polarization and modulation conditions. g_i is the overall gain in signal-to-noise ratio during the measurements; using the Nirvana 2017 detector, in a typical measurement $g_i = 400$. The sign of the rotation and hence that of the Verdet constant can be found by careful inspection of the phase determined by the lock-in amplifier with 180° of phase shift present between positive and negative rotations.

4. Results and discussion

4.1 FePt NPs synthesis and characterization

Four batches of FePt NPs were synthesized by reduction of platinum and iron precursors and the average dcore were measured as 1.9, 4.9, 5.7 and 9.3 nm with narrow size distributions. The TEM images and corresponding size distribution histograms are shown in Fig. 3. After surface modification, the particles had fair stability in polar solvents (e.g. DMF) with no apparent aggregation, ensuring their selective dispersion in the P2VP domain. The particle geometry was observed to undergo a spherical to cubic transition as the particle core diameter increased, consistent with previous work [78,80].

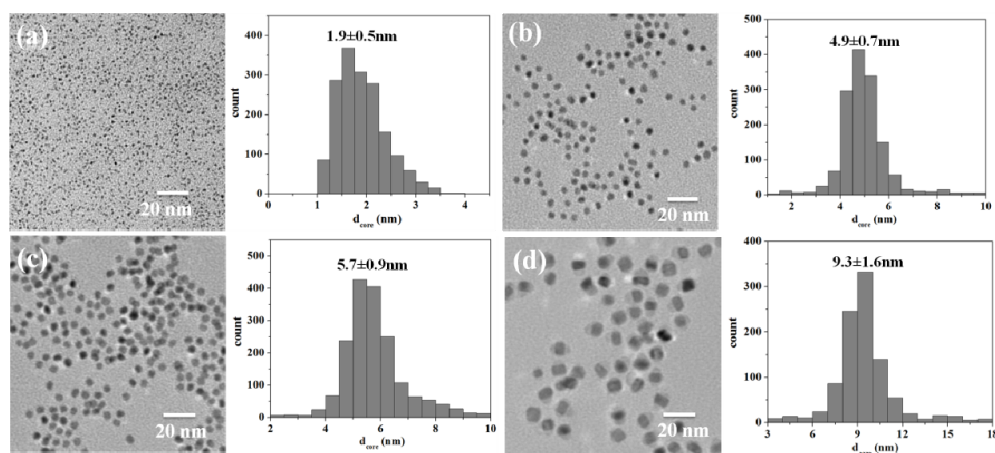


Fig. 3. TEM images of GA capped FePt NPs and corresponding histograms with average core diameter d_{core} (a) 1.9 nm, (b) 4.9 nm, (c) 5.7 nm and (d) 9.3 nm.

The core metal weight fraction of particles and the corresponding volume/filling fractions (f_{NP}) in the BCP were calculated and are provided in Table 1. Among the composites, f_{NP} ranged from 0.02% to 4.8% depending on particle size and loading. f_{NP} was calculated with using the equation $f_{NP} = V_{NP}/(V_{NP} + V_{BCP})$, in which V_{NP} and V_{BCP} referred to NP and BCP volumes accordingly, with the following known or estimated densities: PS-*b*-P2VP ~ 1.05 g/cm³, Fe ~ 7.8 g/cm³, Pt ~ 21.3 g/cm³ and GA ~ 1.7 g/cm³. Fe and Pt atoms pack at a 1:1 mole ratio based on the synthesis protocol [68,81]. NPs with $d_{core} \sim 1.9$ nm had comparatively high volume fraction due to insufficient GA stabilization for small FePt NPs; the excess free ligand was attributed to the low volume fraction compared to other samples. Because no apparent aggregation was observed in polar solvents, the particles are believed to have strong hydrogen bonding interactions with the P2VP domain.

Table 1. FePt NPs core weight and volume fraction (f_{NP} , %) in the nanocomposites

d_{core}^a (nm)	Cor e ^b wt %	f_{NP}^c 0.1wt %	f_{NP} 0.5wt %	f_{NP} 1.0 wt %	f_{NP} 2.5 wt %	f_{NP} 5 wt %	f_{NP} 7.5 wt %	f_{NP} 10 wt %
1.9	30	0.04	0.23	0.46	1.2	2.3	3.6	4.8
4.9	81	0.02	0.12	0.25	0.63	1.3	2.0	2.7
5.7	77	0.03	0.14	0.29	0.73	1.5	2.3	3.1
9.3	85	0.02	0.07	0.16	0.39	0.80	1.2	1.7

^a Average core diameter as analyzed by Image J. ^b Inorganic weight fraction as measured by TGA. ^c Volume fraction of NPs as calculated according to ligand and polymer density.

To further confirm the FePt MNPs structure, both electron and X-ray diffraction were conducted and indicated, as shown in Fig. 4, face centered cubic (fcc) FePt lattice structures with characteristic peaks (111)/(200), (220)/(202) and (311)/(113). The strong and clear ring pattern in the electron diffraction spectra indicated high crystallinity of the FePt NPs. The identical 2θ angle, and the decrease of the full width at height maxima (FWHM) as the particles size increased agreed well with reported work [78–80].

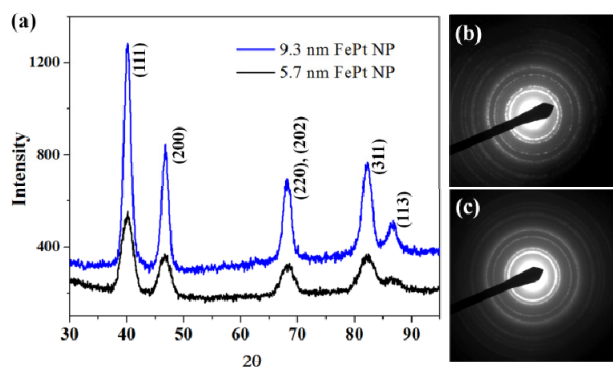


Fig. 4. Crystal structure of size controlled FePt particles: (a) XRD spectrum of $d_{core} \sim 5.7$ nm and 9.3 nm FePt NPs powder, fcc characteristic peaks agree with previous results; (b) $d_{core} \sim 9.3$ nm and (c) $d_{core} \sim 5.7$ nm are electron diffraction images, the halo pattern corresponds to the XRD spectrum calibrated with a gold standard sample.

3.6 FePt NPs/BCP MO composite

SAXS was used to determine the NP/BCP blend morphology and domain spacing (d -spacing). Because paramagnetic materials are temperature sensitive, solvent annealing was adopted to avoid changes in the magnetic properties. As shown in Fig. 5(a), the SAXS 1D profiles of the polymer showed an obvious primary peak at $q^* = 0.087 \text{ nm}^{-1}$ suggesting phase separation of the composite with a d -spacing of 72 nm ($d = 2\pi/q^*$). This primary scattering signal remained apparent upon the addition of NPs indicating a persistent strong phase segregation of NP/BCP blends. The value of q^* shifted to a slightly lower value, indicating that sequestration of NPs began to swell the block.

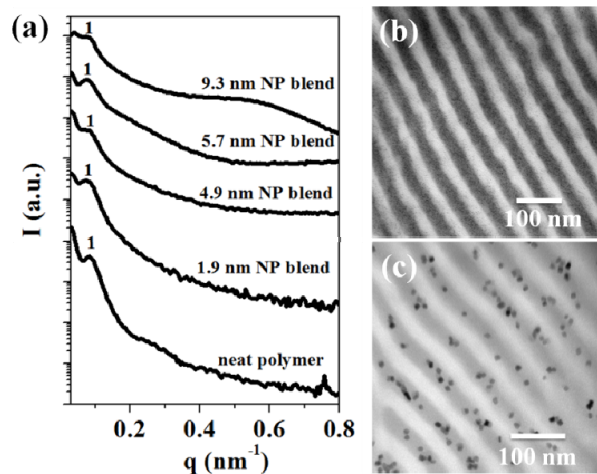


Fig. 5. (a) Room temperature SAXS profiles of neat PS (102 kg/mol)-*b*-P2VP (97 kg/mol) with 1.9 nm, 4.9 nm, 5.7 nm and 9.3 nm FePt NPs at 2.5 wt % loading; primary peaks indicate strong phase separation of NP/BCP blends; representative TEM images of 10 wt % loading of (b) 1.9 nm NPs and (c) 9.3 nm NPs in block copolymer. The P2VP domain was lightly stained with iodine - particles show selective distribution through favorable H-bonding interactions.

Figure 5(b) and 5(c) show that GA capped FePt NPs had selective dispersion in the P2VP domain (dark area stained with iodine). The paramagnetic NPs arrays could be self-assembled into the linear BCP template with particles size less than 10 nm. Although high order reflection was not observed in the 1D spectrum, the TEM images confirmed that well-ordered lamellae morphology was obtained through solvent annealing. The absence of higher order

peaks may result from chain entanglements of high molecular weight BCPs that lead to slow ordering dynamics or from background scattering signals generated from the NPs.

The magnetization of prepared FePt NPs/BCP composites were correlated with increasing core diameter of FePt NPs, shown in Fig. 6. FePt NPs were paramagnetic at room temperature (298 K), consistent with previous studies. There were no differences in magnetization between in-plane and out-of-plane measurement geometries indicating isotropic bulk magnetization in these films. Usually, paramagnetic materials have induced fields along the direction of the applied field, and lose their magnetization upon removal of the field or at elevated temperatures. Paramagnetic NP/BCP composites, due to lack of coercivity, are ideally suited for MO magnetic field sensor applications, and the current study enabled us to choose candidate materials with maximum magnetization. Phenomenologically, the wavelength dependent FR was directly proportional to the available volume magnetization of the transducing material.

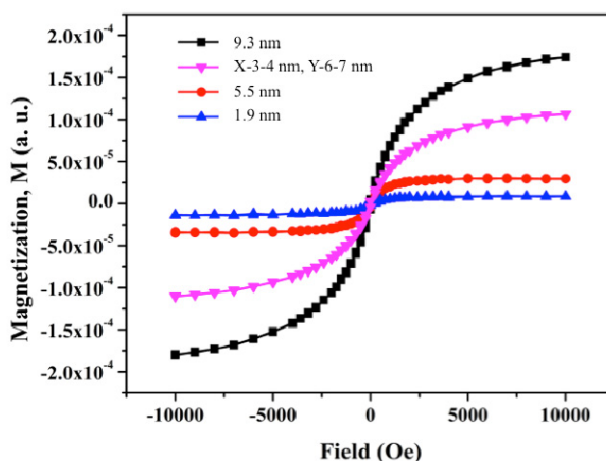


Fig. 6. Hysteresis loops of 2.5 wt % 1.9 nm, 5.5 nm, X = 3-4 nm, Y = 6-7 nm and 9.3 nm FePt NPs in PS (102 kg/mol)-b-P2VP (97 kg/mol) composite. The magnetization falls back to zero in absence of the applied magnetic field for all sizes of particles. The saturation value of magnetization showed clear size dependency.

3.7 Verdet constant measurement of NP/BCP composites

To determine the Verdet constant, the film thicknesses (L) of the composites were determined by surface profilometry. The FePt NP BCP composite films were prepared by drop-casting onto a 3" \times 1" inch glass slide, resulting in long-range thickness variations. The spot size in the FR measurement setup is $< 1\text{ mm}^2$, and measurements were carried out on multiple spots on each film. Given that any error in the thickness measurement directly impacts the calculated Verdet constant, thickness was measured only on the 1 mm^2 segment of film actually used for each of the FR measurements. Thicknesses and corresponding uncertainties were taken into account during Verdet constant calculations and constitute the error bars in data plots (see SI Table S2).

The Verdet constant ($V = \theta/BL$) was determined through FR measurements, in which the total rotation angle of the polarized light, film thickness and applied magnetic field were measured. The FR performance contributed by the 1 mm thick glass substrate was accounted for at each wavelength in the NIR regime and the experimental values for the glass substrate were found to agree well with the existing literature (Table 2) [82].

Table 2. Verdet constants (V) for the glass substrate

Wavelength (λ) (nm)	V ($^{\circ}/\text{T}\cdot\text{m}$)
845	146.8
980	104.0
1310	74.0
1550	39.1

The measured Verdet constants for FePt NP/BCP composites are listed in Table 3. The Verdet constant of NP/BCP composites at 845 nm with 10 wt % loading and $d_{\text{core}} \sim 4.8$ nm FePt particles was as high as -6.3×10^4 $^{\circ}/\text{T}\cdot\text{m}$. This value is comparable with that of BiYIG, with a measured Verdet constant of $\sim 2\text{-}3 \times 10^4$ $^{\circ}/\text{T}\cdot\text{m}$ at 700-800 nm.²⁹ The composite FR response also surpassed TGG, which has V was around $\sim 8 \times 10^3$ $^{\circ}/\text{T}\cdot\text{m}$ at 632 nm.³⁷ The Verdet constant of neat polymer film was measured as $+12$ $^{\circ}/\text{T}\cdot\text{m}$ at 980nm, thus the strong MO response of the NP/BCP composite is introduced by the addition of FePt NPs. Unlike single crystal materials, this high Verdet constant NP/BCP composite was prepared through a solution process, making versatile coating techniques and large area films on flexible substrates possible.

Table 3. Verdet constants (V) of FePt NP/BCP composite films (10^4 $^{\circ}/\text{T}\cdot\text{m}$)^a

wt %/ d_{core}	$\lambda = 845$ nm				$\lambda = 980$ nm			
	1.9 nm	4.8 nm	5.7 nm	9.3 nm	1.9 nm	4.8 nm	5.7 nm	9.3 nm
0.10	-3.82	-5.25	-2.81	-3.18	-2.96	-3.52	-2.16	-2.18
0.50	-3.43	-4.09	-5.25	-2.99	-2.71	-2.95	-3.71	-2.05
1.00	-3.62	-3.27	-4.52	-3.18	-2.87	-2.05	-2.99	-2.27
2.50	-3.20	-3.71	-4.83	-4.42	-2.57	-2.70	-2.81	-3.27
5.00	-4.39	-4.79	-4.79	-5.34	-3.30	-3.46	-3.30	-3.84
7.50	-2.99	-5.51	-4.88	-4.00	-2.58	-4.13	-3.20	-2.35
10.00	-3.61	-6.27	-4.70	-4.40	-2.91	-4.70	-3.29	-3.18
wt%/ d_{core}	$\lambda = 1310$ nm				$\lambda = 1550$ nm			
	1.9 nm	4.8 nm	5.7 nm	9.3 nm	1.9 nm	4.8 nm	5.7 nm	9.3 nm
0.10	-1.09	-2.27	-1.22	-1.35	-1.16	-1.37	-0.37	-0.55
0.50	-0.98	-1.80	-2.21	-1.20	-1.01	-0.96	-0.67	-0.64
1.00%	-0.98	-1.45	-1.93	-1.43	-0.89	-0.91	-0.57	-0.58
2.50%	-0.90	-1.66	-2.07	-1.94	-0.90	-1.01	-0.62	-0.80
5.00%	-1.14	-2.10	-2.06	-2.25	-1.15	-1.26	-0.65	-0.79
7.50%	-0.91	-2.33	-2.10	-1.77	-0.90	-1.48	-0.68	-0.67
10.00%	-1.02	-2.79	-2.08	-1.90	-0.99	-1.74	-0.77	-0.70

^a The given weight percentages include the capping layer of GA.

The figure of merit FOM for MO materials in the unsaturated regime is given by

$$FOM = \frac{V(^{\circ}/\text{Tm})}{\alpha(\text{m}^{-1})} \quad (3)$$

in which the Verdet constant (V) is divided by the absorption coefficient (α); the FOM accounts for the trade-off between Faraday rotation and optical loss. In Fig. 7 we plot the FOM vs. the number density of NPs, where the absorption coefficient was measured by UV-vis spectroscopy and the number density of NPs was calculated according to size distribution and TGA data. FOM values are essential in determining the practical usefulness of materials for nonreciprocal MO devices as it includes information about optical loss. Materials with excellent FR performance but low light transmission can only be used in applications suitable for very thin films.

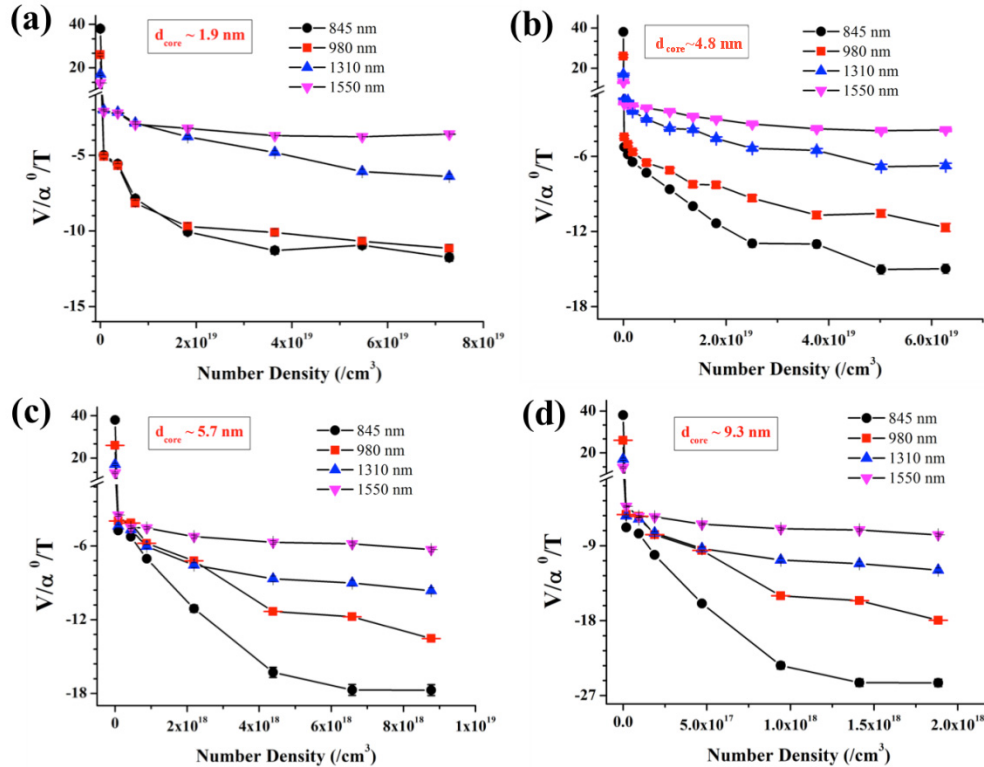


Fig. 7. The MO figure of merit (FOM) plotted vs. number density for particle sizes (a) 1.9 nm, (b) 4.8 nm, (c) 5.7 nm and (d) 9.3 nm at the four wavelengths studied. The FOM was calculated from Verdet constant and film absorption coefficient, which was determined by UV-vis spectroscopy (see SI Table S3-S6). Particle number density was calculated based on NP size and TGA data.

The NP/BCP composites discussed above exhibited both relatively high value of V and FOM, indicating excellent MO response and transparency. For instance, the Verdet constants of most NP/BCP composites at 845 nm were 10 times larger than those of composites made by sol-gel methods, which provided a maximum $V \sim 4000\text{-}5000$ $^{\circ}/\text{T}\cdot\text{m}$ near 680-780 nm [37,44]. The maxima of FOM value of the 9.3 nm composite was as high as ~ 27 $^{\circ}/\text{T}$ at 845 nm, 1.5 times higher than that of BiYIG single crystal at 760 nm [29].

Clearly the MO properties of the particles provide the excellent FR performance as the FR response from neat BCP films was negligible. We also note the large values of the FOM for neat polymer with relatively low Verdet constant paired with extremely low absorption coefficient; this is a result of the definition of the FOM and would generally lead to device geometries with impractically long path lengths. In addition, Fig. 7 shows the change in magnetic behavior from the diamagnetic neat polymer to paramagnetic NP/BCP composite, accompanied by a V value transition from positive to negative sign. The nanostructure of the NP/BCP blends is believed to play a critical role in the MO performance due to the evident selective NP sequestration and consequent control over the particle distribution and aggregation compared to the homopolymer system [34]. The Verdet constant of homopolymer blend is 1-2 magnitude (see SI Table S1) lower compared to NP/BCP blends under the same measurement conditions, further supporting this picture.

There are several points to be noted with respect to the V and FOM values of the NP/BCP composites. First, paramagnetic materials typically show a negative V and FR dispersion strongly depends on their optical band gap, in the absence of which the FR response varies as

λ^{-2} [3]. The FOM values for all the samples decreased at longer wavelengths, consistent with this theory. The Verdet constant decreased by 3-6 times from $\lambda = 845$ nm to $\lambda = 1550$ nm for FePt NP/blend samples. The wavelength dependence of the Verdet constant and the FOM was typical for polymeric composites, where the primary factor influencing the dispersion was the proximity and strength of the lowest energy NP absorption band. This simple dependence further points to the optical quality of the composites, since the performance is not dominated by Rayleigh scattering, which has a λ^4 contribution to the FOM.

Secondly, the loading of NPs clearly played a role in determining FR performance. Although there were composite-to-composite variations in how the wavelength dependent Verdet constant changed with particle loading, the absolute values of FOM increased with number of density until saturation occurred. Specifically, the FOM values of $d_{core} \sim 5.7$ and 9.3 nm composites saturated at very low number density at $\lambda = 1550$ nm, additional particle density failed to further increase the magnitude of the FOM of the composite. Usually, this type of saturation behavior for composites is attributed to aggregation of NPs and subsequent light losses from scattering. However, we observed that the Verdet constant increased more rapidly than the absorption coefficient with number density. We conclude that the earlier onset of saturation phenomenon for the larger particles may be attributed to the larger NPs more rapidly filling and less optimally packing the P2VP polymer domains with similar number density. This sub-optimal domain matching may also be a factor in the smaller absolute Verdet constants measured for films incorporating larger diameter NPs.

Finally, the particle size exhibits clear effects on the FR rotation response. Composites incorporating smaller NPs, such as 2 nm and 4.8 nm NP films, showed 1.5-2 times larger V than other samples at the same wavelength and loading, while also exhibiting comparable FOM values with similar number density. Considering the same volume fraction, smaller NPs usually had much higher number densities than the larger NPs, potentially leading to decreased inter-particle distance and increased scattering losses. As a result, FOM values at some wavelengths were comparable or even lower for small NPs composites than for larger NP composites, despite better absolute FR response.

In general, the BCP template offered periodic structure and strong NP/BCP interaction facilitating specific magnetic NPs distribution at the nanoscale with modest FePt nanoparticle surface modification. Through fine control over particle surface modification and distribution in specific domains, the directed self-assembly of BCP/NP blends exhibited significantly improved MO response and transmission. The solution processable method also enables the fabrication of functional hybrid materials by various coating techniques on flexible substrates, providing the possibility of roll-to-roll processing for large area MO devices applications.

5. Conclusions

We have demonstrated that the self-assembly of magnetic NPs and BCPs provides an effective strategy toward MO materials with Verdet constants up to $\sim 10^4$ °/T-m in the NIR regime at room temperature. The magnetic NPs introduced improved the FR performance, as neat polymer only had $V \sim 12$ °/T-m under the same conditions. The Verdet constant of NP/BCP blends decreased with increased measurement wavelength, consistent with paramagnetic composite behavior. The hybrid material also exhibited saturation behavior and this phenomenon was attributed to increased optical scattering introduced by the higher particle concentrations in confined domains. In general, this method provides a simple route toward fabricating high-performance MO material through a solution process. By controlling the specific structure of the BCP templates and surface functionality of particles, these functional hybrid materials provide an exciting tool for a myriad of MO applications.

Funding

National Science Foundation (NSF) Center for Hierarchical Manufacturing (CMMI-1025020).

Acknowledgment

The authors would like to acknowledge support from The Materials Research and Engineering Center at University of Massachusetts, Amherst and The College of Optical Sciences, at University of Arizona.